Unsteady multi-parameter flow diagnostics by filtered Rayleigh scattering: system design by multi-objective optimisation

Ulrich Doll[1,*], Ingo Röhle[2], Michael Dues[3]
1: Experimental Thermal Hydraulics Group, Paul Scherrer Institute (PSI), Switzerland
2: Berliner Hochschule für Technik, Germany
3: ILA R&D GmbH
* Correspondent author: ulrich.doll@psi.ch

Keywords: filtered Rayleigh scattering, multi-objective optimisation, Monte-Carlo simulation, unsteady flow measurement, simultaneous, pressure, temperature, flow velocity, multiple views

ABSTRACT

The measurement of the time-resolved three-component (3C) velocity field together with scalar flow quantities such as temperature or pressure by laser-optical diagnostics is a challenging task. Current approaches typically employ combinations of different methods relying on tracer particles or molecules, which requires elaborate calibration procedures of the tracer's photo-physical properties and extensive instrumentation. In contrast to this, the tracer-free filtered Rayleigh scattering (FRS) technique has been proven to obtain combined time-averaged velocity and scalar fields and might offer a viable alternative for unsteady flow diagnostics. By applying multiple perspective views, two detection system variants are presented, combining 1) six observation branches with one camera/molecular filter and 2) four camera views with two cameras and molecular filters of differing vapour densities. Both configurations in principle allow for the simultaneous measurement of instantaneous 3C velocity, temperature and pressure fields. Multi-objective optimisation is used to enhance the detection setups for different sets of experimental configurations. It is shown that a higher number of observation positions and the associated dynamics of the FRS signal prove to be advantageous compared to the use of less views in combination with two acquisition channels equipped with different molecular filters. It is also demonstrated that the use of linearly polarised laser light is preferred over circular polarisation. Future work will focus on the realisation of the multiple-view FRS concept for the combined measurement of 3C velocity and scalar fields.

1. Introduction

To this day, numerous different laser-optical techniques to measure flow velocity or scalar quantities (e.g. temperature, density, pressure, concentration) have been developed. However, most of these methods are limited to the measurement of a single flow quantity such as velocity, temperature or concentration, which is generally not sufficient to understand the multi-dimensional nature of complex turbulent thermo-fluid systems. To further enhance the information content of their measurements, experimentalists strive to measure multiple flow variables simultaneously by combining different laser-optical techniques. This becomes

increasingly challenging when the turbulent interaction between velocity and scalar fields is to be characterised. Experimental approaches to date include the combined use of particle image velocimetry (PIV) with tracer laser induced fluorescence (LIF) (Su & Mungal, 2004; Jainski et al., 2014; Klinner & Willert, 2017), laser induced phosphorescence (LIP) (Lee et al., 2016; Schreivogel et al., 2016; Straußwald et al., 2020), or filtered Rayleigh scattering (FRS) (McManus & Sutton, 2020; Most et al., 2002) to measure velocity, temperature, or concentration fluctuations to derive higher order scalar transport correlations. All of these approaches have in common that they rely on foreign tracer particles or molecules and, therefore, require careful tracer selection with respect to aerodynamic and photo-physical properties as well as a thorough calibration procedure for each experiment. Furthermore, extensive instrumentation with at least two laser systems and a minimum of two or more cameras is needed.

The complexity of current tracer-based state-of-the-art experimental approaches imply an urgent need for innovative and practical approaches that can be applied to a wide range of research questions, while only requiring a minimum of modifications towards the actual experiment. A promising candidate to fill this gap is the FRS technique. When applied stand-alone, the method requires no tracer particles/molecules to be added to the flow, but solely relies on the elastic scattering of laser light from gas molecules already present in the plane of interest. Since Rayleigh scattering holds information on flow velocity, temperature, pressure and density inside the probe volume, the FRS method has the potential to measure all of these quantities simultaneously (Forkey et al., 1996; R. Miles & Lempert, 1990). To exploit the FRS technique's capabilities for measuring multiple flow quantities, a frequency scanning FRS method was previously introduced that enables the simultaneous measurement of time-averaged pressure, temperature and velocity fields (Boguszko, 2003; Doll et al., 2014a; Forkey et al., 1996). By using continuous wave laser light with excellent spectral properties, the technique could be used in a wide range of applications, from precision laboratory experiments (Doll et al., 2015, 2016) to turbomachinery component testing under realistic operating conditions (Doll et al., 2012, 2018; Doll, Stockhausen, Heinze, et al., 2017; Schroll et al., 2017). The FRS velocimetry approach further extends the capabilities of the frequency scanning method to the combined measurement of three-component (3C) velocity and scalar fields by using image-fibre bundle technology to realise varying camera views (Doll, Stockhausen, & Willert, 2017). However, since an image has to be taken at each frequency step, the frequency scanning procedure is rather time consuming and cannot be applied to acquire unsteady flow field data.

In contrast to frequency scanning FRS, the combined measurement of unsteady flow velocity and scalars will have to rely on high energy pulsed laser radiation. To derive multiple instantaneous

flow quantities from a single-pulse FRS measurement, additional experimental information must be obtained. In case of a single-component gas flow, the FRS signal is a function of the five[1] unknown flow variables (three velocity components, temperature, pressure). A possible concept for the simultaneous measurement of all these quantities involves the further development of the aforementioned FRS velocimetry method: By illuminating the plane of interest with a single laser pulse (at a single excitation frequency) and observing the flow field using a multiple-branch image fibre bundle from several different directions. Consequently, the measured Doppler frequency shifts (which contain the velocity information) recorded through the different fibre bundle branches vary, while the temperature and the pressure information for each bundle position remains the same (Doll, Stockhausen, & Willert, 2017; Nobes et al., 2004; Willert et al., 2005). Such a dataset can then potentially be used to derive instantaneous 3C velocity, temperature and pressure fields at each resolution element.

The following analysis aims at identifying the optimal detection configuration to maximize sensitivities of a single-pulse FRS measurement to the pertinent flow variables pressure, temperature and the three components of velocity. Two detection setups, combining one iodine absorption filter cell/camera with six views and two iodine absorption filter cells/cameras with four views are considered and multi-objective optimisation is used to determine the best set of camera positions. After introducing the general conception of the detection units, a detailed overview on FRS signal modelling and parameter dependencies is provided. This is followed by a description of the optimisation framework including the underlying assumptions and constraints. Finally, the optimisation results are discussed and interpreted and design criteria for an optimal single-pulse multi-view FRS detection configuration are derived.

2. Detection concepts

Any FRS acquisition and evaluation method is concerned with the multiple parameter dependency of the measured signal. One measured intensity value stands against up to five unknown flow quantities (3C flow velocity, temperature, pressure). In addition, a minimum of three linear independent observation directions is required to derive the three components of the velocity vector. To simultaneously measure multiple time-averaged flow variables, the frequency scanning method can be used. To realize the simultaneous measurement of multiple flow quantities using pulsed laser radiation, time consuming frequency scanning cannot be applied, but the FRS signal's dependency on the scattering angle can be exploited. Two approaches towards

[1] An equation of state is typically applied to couple density with pressure/temperature

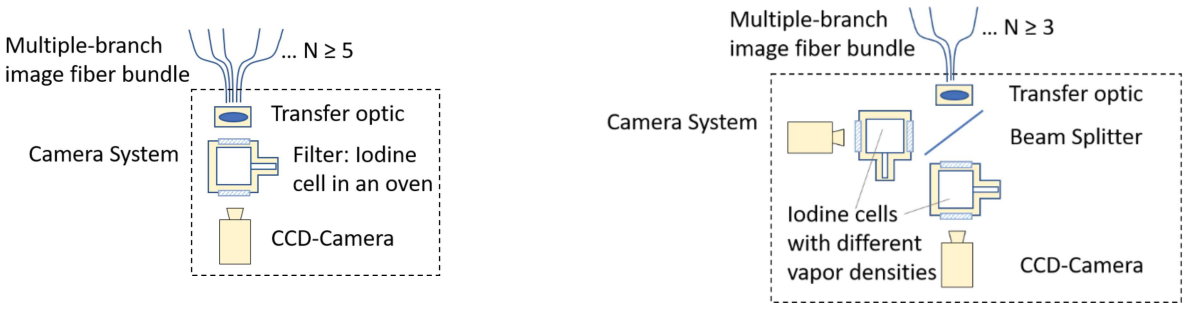

Figure 1 Possible variants of an FRS-camera system setup.

an FRS camera system suitable to perform multi-parameter time-averaged or single-pulse FRS measurements are shown in Figure 1. Regarding instantaneous FRS, the first approach (Figure 1, left: Cam. 1) requires a minimum of five observation branches to unambiguously derive all flow quantities (three velocity components, temperature and pressure). The second approach (Figure 1, right: Cam. 2) uses two acquisition channels as indicated by the two cameras, each equipped with an absorption filter of differing vapour concentration. Such a configuration would require a minimum of three observation directions, which results in six independent intensity values to derive the five unknown flow quantities. In case of time-averaged measurements using frequency scanning, the number of observation branches could be reduced to three for both configurations.

3. FRS signal modelling and influencing variables

The determination of a single flow quantity or multiple flow quantities from an FRS dataset relies on a non-linear measurement model. For a mono-component gas (air can be treated as one), the overall FRS signal intensity detected at a sensor element of the camera at excitation frequency k and camera position l can be written as (Doll et al., 2014a; Doll, Stockhausen, & Willert, 2017; Forkey, 1996; R. B. Miles et al., 2001):

$$S_{kl}\left(\nu_{0,k}, p, T, \Delta\nu_l, \theta_l\right) = C_l I_0 n \sin^2\phi_l \int_{-\infty}^{\infty} r_l\left(\nu - \nu_{0,k}, p, T, \Delta\nu_l, \theta_l\right) \tau(\nu)\, d\nu. \quad \textbf{(1)}$$

The experimental parameter C describes the optical efficiency of the setup for each camera position. The incident laser intensity is denoted by I_0, the number density of the molecules involved in the scattering process is n. The electric field of laser light scattered from a small particle in the Rayleigh regime is typically described as an oscillating dipole. The $\sin^2\phi$ term accounts for the projection of the dipole field amplitude on the observation direction (R. B. Miles et al., 2001). According to the scattering geometry shown in Figure 2, $\phi = \cos^{-1}(\vec{o}\cdot\vec{p})$ is the angle between polarisation direction $\vec{p}$ of the incident laser light along $\vec{l}$ and observer direction $\vec{o}$. In the depicted case, $\vec{l}$ and $\vec{p}$ are orthogonal and both are located in the x-y-plane, so that $\vec{p} = (-l_2, l_1, l_3)$. The

integral expression refers to the convolution of the Rayleigh scattering's spectral lineshape r and the molecular filter's transmission curve τ. The convolution term includes the dependencies of the measured signal with respect to the laser's output frequency ν_0, pressure p, temperature T as well as Doppler frequency-shift (due to flow velocity) $\Delta\nu$. The relationship between Doppler frequency shift and flow velocity is expressed by the Doppler formula

$$\Delta\nu_l = \frac{\nu_0}{c}\left(\vec{o}_l - \vec{l}\right)\cdot\vec{\mathrm{v}}\,, \tag{2}$$

with c as the speed of light and $\vec{\mathrm{v}}$ as the three-component flow velocity vector. For an observation with multiple camera views, Equation (2) can be reformulated as matrix operation, so that

$$\Delta\vec{\nu} = \frac{\nu_0}{c} M\cdot\vec{\mathrm{v}}\,,$$
$$\Delta\vec{\nu} = \begin{bmatrix}\Delta\nu_1\\ \vdots\\ \Delta\nu_N\end{bmatrix}, M = \begin{bmatrix} o_{1,x}-l_x & o_{1,y}-l_y & o_{1,z}-l_z\\ \vdots & \vdots & \vdots\\ o_{N,x}-l_x & o_{N,y}-l_y & o_{N,z}-l_z\end{bmatrix}, l = 1\ldots N \tag{3}$$

with N being the number of camera views. In addition, the scattering angle $\theta = \cos^{-1}(\vec{o}\cdot\vec{l})$ between observation and laser direction incorporates the dependency of the Rayleigh lineshape on the scattering geometry. It should be noted that the Rayleigh lineshape is also influenced by the excitation frequency. However, this influence can be neglected for the envisaged narrow laser frequency range. Finally, the shape of the molecular filter's transmission curve in relation to the laser's output frequency has a significant impact on the detected FRS signal intensities and the resulting flow variable sensitivities.

Two simulated iodine transmission spectra (Forkey et al., 1997) are shown in Figure 3, left. There, the so-called saturation temperature T_{sat} defines the temperature at which the iodine content of the filter cell has evaporated. A higher saturation temperature involves a higher iodine vapour density inside the filter cell, which results in a stronger filter effect due to an increase in background (continuum) absorption and individual line strength. The latter has a very pronounced effect on the minimal achievable transmission, which increases by several orders of magnitude from 70°C to 75°C saturation temperature and is the key quantity for the suppression of unwanted laser stray light or Mie scattering. However, the accompanying increase in background

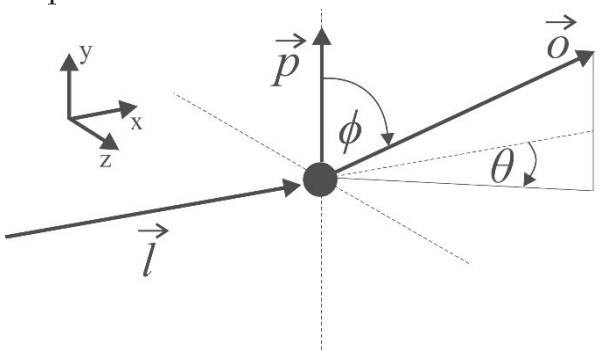

Figure 2 The laser is incident along $\vec{l}$ and linearly polarized along $\vec{p}$. Laser light is scattered from a particle (molecule) in observation direction $\vec{o}$. The angles between polarisation/observer and laser direction/observer are ϕ and θ.

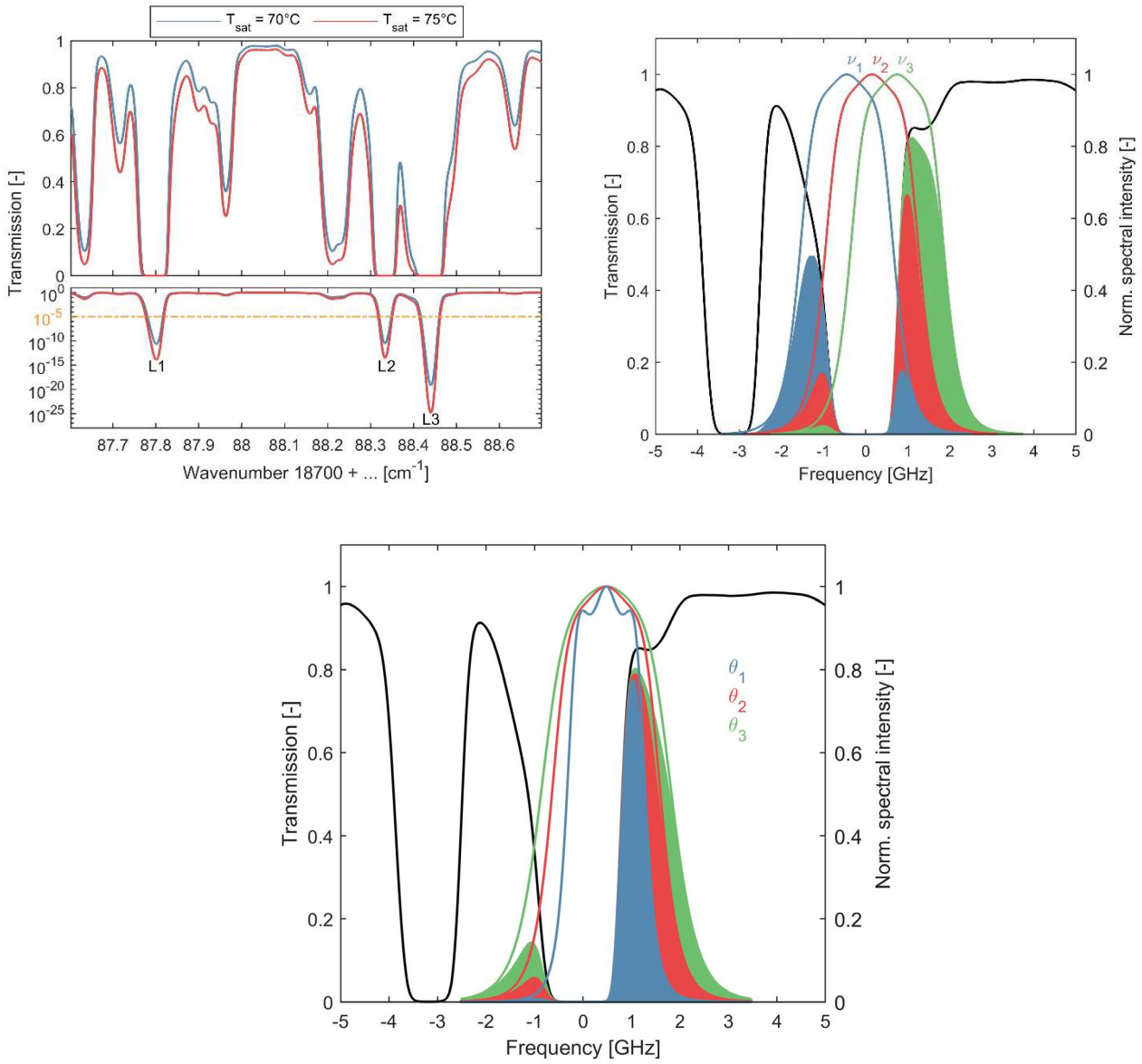

Figure 3 (Left) The top graph shows a comparison two simulated iodine filter transmission curves with saturation temperatures (T_{sat}) of 70°C (blue) and 75°C (red). The bottom graph depicts the same filter lines in logarithmic scale. The 10^{-5} transmission level is indicated by the dashed-dotted line (yellow). Potentially suitable absorption lines are marked with L1, L2 and L3. (Right) Varying the laser frequency along the iodine transmission curve leads to different spectral portions of the Rayleigh scattering that are transmitted through the filter. (Bottom) Similar, a variation of the scattering angle alters the spectral shape and thereby the transmitted FRS signal.

absorption lowers the overall intensity of the FRS signals. In order to reach a sufficient attenuation of laser stray light and Mie particle scattering, a minimal transmission of 10^{-5} is required (Doll et al., 2014a). The effect of the laser's output frequency on the FRS signal is depicted in Figure 3, right. The three selected frequencies are located on the left (blue), on the right (green) and at the

absorption minimum (red). Distinct differences of the spectral portions of the Rayleigh scattering spectrum that are transmitted through the iodine filter can be observed. Similar to that, a variation in the scattering angle θ alters the Rayleigh scattering's spectral lineshape and, thereby, the transmitted FRS signal.

4. Optimisation framework

The previous section provides an overview of the multi-variate dependency of the FRS signal on scattering geometry, iodine filter properties and laser frequency. On the one hand, this offers a huge optimisation potential. However, in view of the intended usage of multiple camera views to simultaneously measure different instantaneous flow variables and the resulting complex scattering geometry, the following analysis focuses on optimising the camera positions such that measuring sensitivities for the three velocity components, static pressure and temperature are maximised.

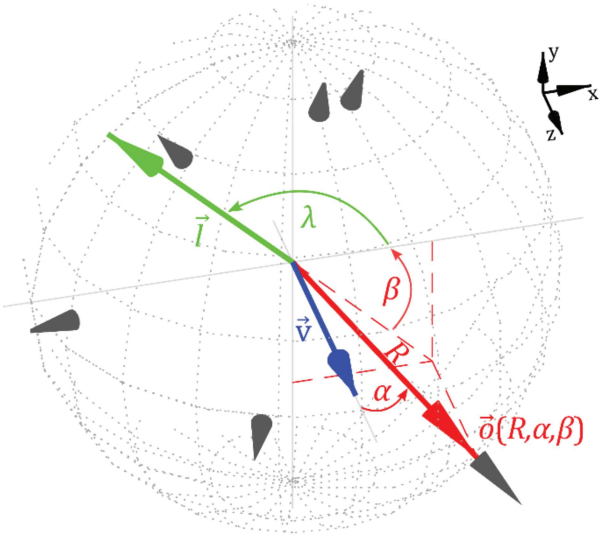

Figure 4 Geometrical definitions used for the optimisation. The laser propagates along $\vec{l}$ in the x-y-plane, the laser direction is defined by the angle λ. The grey cones represent the different camera positions along $\vec{o}$, oriented on a spherical surface. Positions are defined in spherical coordinates by the sphere radius R and angles α, β. The flow velocity $\vec{v}$ is mainly oriented along the z-axis.

The geometrical definitions and constraints implemented within the optimisation routine are depicted in Figure 4. The laser propagates along $\vec{l}$ in the x-y-plane and the orientation of the laser in this plane is determined by the angle λ, which rotates around the z-axis in counter-clockwise direction. The different image fibre bundle front-end positions are indicated by the grey cones. Owing to restrictions imposed by the test rig geometry, observation positions are constrained to the area downstream of the AIP. To provide constant magnification (it is assumed that each view uses the same light collection optics), all camera views are positioned on a spherical surface with radius R. By using spherical coordinates, each camera position then can be explicitly described by the polar and azimuthal angles α and β. In previous studies on theDoppler Global Velocimetry (DGV) technique based on multiple viewing directions, it was shown that the resulting velocity measurement error depends on i) the uncertainty of each individual Doppler velocity component, ii) the transformation to orthogonal velocity components using the inverse of the sensitivity matrix M of Equation (3) and iii) the orientation and magnitude of the flow velocity itself (Charrett et al., 2007). It was concluded that lowest velocity uncertainties are obtained when the different camera

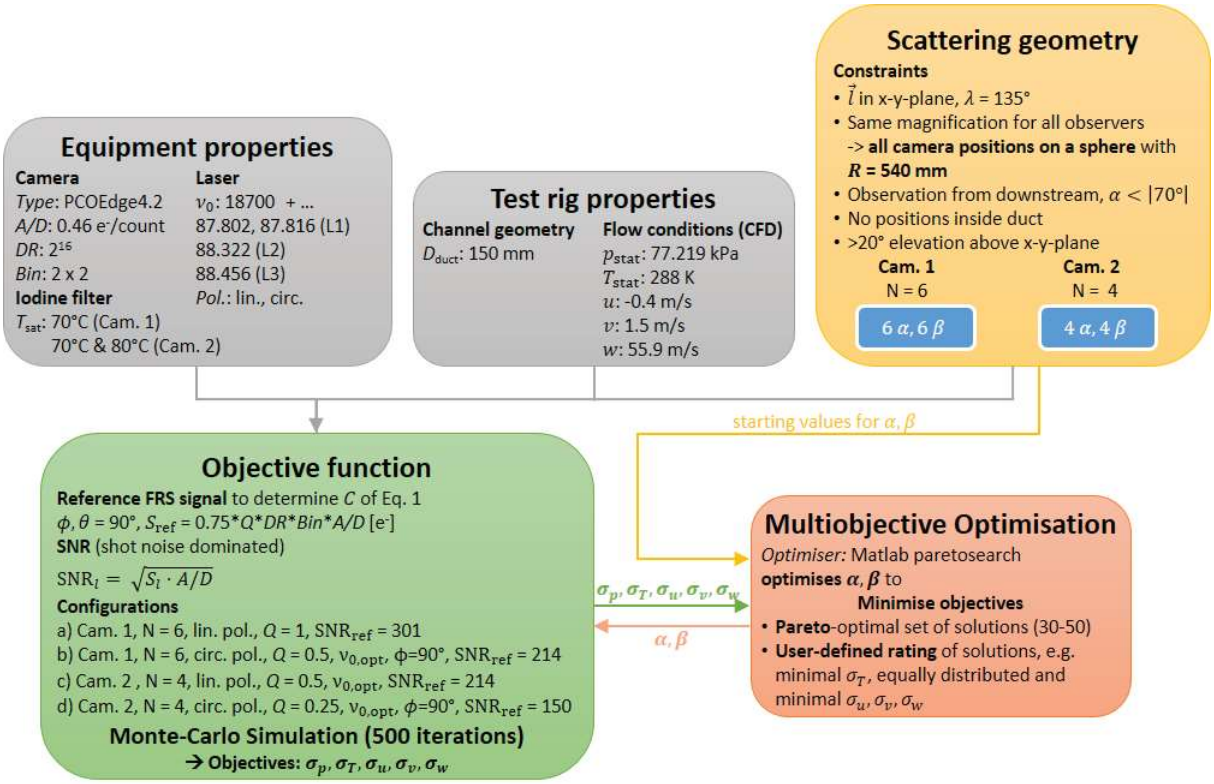

Figure 5 Flow chart of the optimisation framework

views are well spread (Charrett et al., 2007; Nobes et al., 2003). Even though in FRS the two additional thermodynamic quantities pressure and temperature have to be considered and the convolution of Rayleigh lineshape and iodine transmission curve brings additional complexity, these considerations should also be transferable to FRS to a certain extent. For the current application with the main velocity component along the z-axis, it is beneficial to orient the laser at an angle of 45° to the x- and y-axis, so that the resulting velocity uncertainties for u and v components are evenly distributed.

A flow chart describing the optimisation procedure is shown in Figure 5. The objective function used in the optimisation is founded on a Monte-Carlo simulation approach introduced for FRS uncertainty quantification (Doll et al., 2014b, 2016). The objective function receives input from three different domains that are related to the experiment encompassing camera properties, laser excitation wavenumber, direction pf polarisation, iodine filter transmission, the test rig geometry and flow conditions as well as the previously described scattering geometry. All of these input parameters influence the actual FRS signal level and the associated signal-to-noise-ratio (SNR). In the first step, the calibration constant C of Equation (1) has to be determined. For this purpose, a reference signal for a single observer S_{ref} for a defined scattering geometry (ϕ, θ = 90°) is calculated within the objective function for each experimental configuration a)-d). The reference signal level is predefined for Cam. 1 and linear polarised laser light to 75% of the camera's available dynamic

range (DR). Additionally, spatial binning is applied to further increase SNR (Bin). The factor Q takes into account configuration-dependent specifics of the camera module and polarisation state of the laser light; for example, circular polarisation is assumed for configuration b), so that only half of the signal level (Q = 0.5) reaches the detector compared to configuration a) with linear polarisation. The second acquisition channel (50:50 split) in configurations c) with linear and d) with circular polarisation results in Q-values of 0.5 and 0.25, respectively. S_{ref} is then used to infer the calibration constant C in an iterative process. By switching back to multiple observers using the α_l, β_l-angles provided by the optimiser, Equation (1) is used to create an artificial FRS dataset based on the specified flow conditions. For the assumed signal levels, shot noise dominates the noise statistics, so that the SNR for each camera view can be calculated from $\mathrm{SNR}_l = \sqrt{S_l \cdot A/D}$. Based on the derived SNR, Gaussian noise is added to the simulated intensities. In the next step, the evaluation algorithm attempts to retrieve the original flow parameters from the artificially noisy FRS dataset. The procedure is repeated 500 times and standard deviations for the five flow quantities are deduced from the resulting probability distributions as a measure of the parameter sensitivity of each flow variable. The resulting $\sigma_p, \sigma_T, \sigma_u, \sigma_v, \sigma_w$ are then passed to the optimiser, which, in an iterative procedure, tries to minimise these objectives by adapting the α_l, β_l-angles. The optimiser used in this study is the Matlab paretosearch algorithm for multiobjective optimisation. The solver generates a collection of Pareto-optimal (non-dominated) solutions on a multi-dimensional trade-off surface (Pareto front) spanned by the set of objectives (Collette & Siarry, 2004). From the obtained set of solutions, one or more are chosen by applying user-defined selection criteria; however, each of these decisions, e.g. selecting the optimal solution for a single objective will, lead to a trade-off with respect to the other objectives.

5. Optimisation results and discussion

Variation of excitation wavenumber In Section 3 it is argued that the laser's output frequency, i.e. the spectral positioning of the laser line in relation to the selected absorption feature, has a large impact on the FRS signal level. Three of the absorption lines and associated wavenumber ranges shown in Figure 3 contain potentially suitable measuring wavenumbers for FRS. The equipment properties box in Figure 5 includes the actual wavenumbers that were successively selected as input variables for the optimisation. The two first wavenumbers are located in the centre and to the right of absorption line L1. The wavenumber at L2 is shifted to the left, the one at L3 to the right of the respective transmission minimum. The reason for omitting the central positions for L2 and L3 is that the width of these absorption lines is too large at the selected saturation temperatures/iodine vapour densities, so that most of the Rayleigh scattering is blocked and almost no signal is received at the detector. All selected wavenumbers fulfil the 10^{-5}

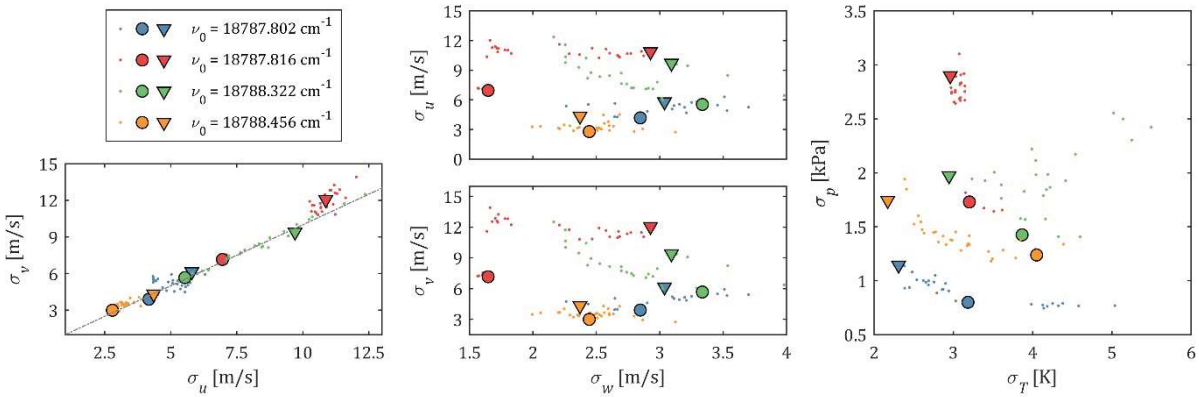

Figure 6 Representation of the trade-off surface (Pareto front) for varying excitation wavenumbers. Dot symbols embody the entire set of Pareto-optimal solutions, circle and triangle symbols indicate user-selected solutions according to velocity and temperature selection criteria. The grey dashed-dotted line in the left panel indicates perfect symmetry.

transmission criterion. The wavenumber variation is carried out for configuration a) of Figure 5 only and it is presumed that the results are transferable to the other configurations as well.

A representation of the objective solution space for the selected wavenumbers is shown in Figure 6. The coloured dots represent all objective function values from the Pareto-optimal set of solutions. The panel on the left depicts the standard deviations of the two transverse velocity components plotted against each other; the two panels in the centre depict each of these components versus the standard deviation of the main velocity component. The panel on the right contains similar information on pressure and temperature. As previously indicated, the orientation of the laser at 45° with respect to the x- and y-axes leads to an almost perfect symmetry (grey dashed-dotted line) between u and v sensitivities. The respective standard deviations σ_u and σ_v span a range from 2.5 to 15 m/s. The lowest values are obtained at an excitation wavenumber of 18788.456 cm^{-1} and the worst performance is observed at 18788.816 cm^{-1}. In contrast to σ_u and σ_v, the spread of σ_w of the main flow component is much smaller for all laser output wavenumbers and lies within a range of 1.5 to 4 m/s. The wavenumbers 18787.802, 18787.816 and 18788.456 cm^{-1} present sensitivities at a comparable level, the σ_w values at 18788.322 cm^{-1} are about 1 m/s higher on average. While the flow velocity exhibits the best results at an excitation wavenumber of 18788.456 cm^{-1}, pressure and temperature standard deviations are lowest at 18787.802 cm^{-1}, with values varying between 0.7 to 1.1 kPa and 2 to 3 K, respectively. The σ_p and σ_T range from 1.3 to 1.6 kPa and 3 to 4 K at 18788.456 cm^{-1} and exceed 1.5 kPa and 3 K for the remaining two laser output wavenumbers.

Following these general observations on the complete set of Pareto-optimal solutions, the selection of an appropriate configuration of camera views from this set is discussed below. Within the framework of the selection strategy, two main goals are formulated: 1) With respect to flow velocity, the individual standard deviations σ_u, σ_v and σ_w should be as low as and their spread as small as possible. 2) Temperature sensitivity should be as high as possible. Both selection criteria are reflected in terms of programming by the following relationships:

Velocity criterion:
$$\min\left(\text{mean}\left(\begin{bmatrix}\sigma_u\\ \sigma_v\\ \sigma_w\end{bmatrix}\right) + \text{std}\left(\begin{bmatrix}\sigma_u\\ \sigma_v\\ \sigma_w\end{bmatrix}\right)\right) \quad \textbf{(4)}$$

Temperature criterion:
$$\min(\sigma_T) \quad \textbf{(5)}$$

Both criteria are applied to the set of solutions obtained at each excitation wavenumber. The results are indicated by the circle (velocity criterion) and triangle (temperature criterion) markers in Figure 6. The distribution of the markers confirms the previous observation that the best overall flow parameter sensitivities are obtained for an excitation at 18788.456 cm^{-1}. When applying the velocity criterion, σ_u, σ_v and σ_w take uniform values of about 2.4 to 3 m/s. Temperature and pressure lies at 4.1 K and 1.2 kPa, respectively. These values slightly change when the temperature criterion is applied. Regarding velocity, an asymmetry is introduced between the components, with an increase in σ_u and σ_v to 4.4 m/s and 4.3 m/s and a decrease in σ_w to 2.4 m/s. Likewise, σ_p subtly rises to 1.7 kPa, while σ_T falls to 2.2 K. A further increase in pressure sensitivity can be achieved when the temperature criterion is applied to the solutions obtained for the excitation wavenumber at 18787.802 cm^{-1}, reducing σ_p to 1.1 kPa at similar σ_T. This is, however, penalised with a significant decrease in velocity sensitivities of the transverse components u and v. Sensitivities for all excitation wavenumbers after applying the both selection criteria are summarised in Table 1.

Table 1 Flow parameter sensitivities for velocity and temperature selection criteria

Criterion	ν_0 [cm^{-1}]	σ_p [kPa]	σ_T [K]	σ_u [m/s]	σ_v [m/s]	σ_w [m/s]
Velocity	18787.802	0.8	3.2	4.2	3.9	2.8
	18787.816	1.7	3.2	7.0	7.2	1.6
	18788.322	1.4	3.9	5.5	5.7	3.3
	18788.456	1.2	4.1	2.8	3.0	2.4
Temperature	18787.802	1.1	2.3	5.8	6.2	3.0
	18787.816	2.9	3.0	10.9	12.1	2.9
	18788.322	2.0	2.9	9.7	9.4	3.1
	18788.456	1.7	2.2	4.4	4.3	2.4

The respective optimised camera positions after applying the selection criteria for the excitation wavenumbers at 18787.802 and 18788.456 cm^{-1} are shown in Figure 7. It becomes apparent that for both wavenumbers the bulk of the optimised camera views is oriented in forward scattering. In addition, the majority of optimised views are located close to or at the limits imposed by the geometrical constraints (black dotted lines). This means that the optimiser generally tries to approach extreme angles to minimise the objectives, which is consistent with the previous observation made for DGV that it is beneficial to provide a wide spread of camera views to achieve high velocity sensitivities (Charrett et al., 2007; Nobes et al., 2003). Overall, it is difficult to establish a universal design rule for selecting the best camera views to achieve the highest flow parameter sensitivities. This is not surprising, since in the present case the optimiser maps a five-dimensional objective space by varying twelve angles corresponding to the six camera views. In the following, the excitation wavenumber at 18788.456 cm^{-1} is selected and used in the further investigations.

Comparison of configurations a)-d) The typical FRS experiment is based on narrow-bandwidth linearly polarised laser light. The linear polarisation gives rise to the typical angular dipole distribution of the Rayleigh scattering intensity, which is expressed through the $\sin^2\phi$ dependency in Equation (1). For the intended usage of multiple observation directions distributed around the test object, it might prove advantageous to use circularly polarised laser light instead. By using laser light with circular polarisation, all camera views receive the same amount of Rayleigh scattering intensity, which is, however, reduced to 50% of the maximum value that could be achieved with linearly polarised light at ϕ = 90°. To investigate the influence of the polarisation

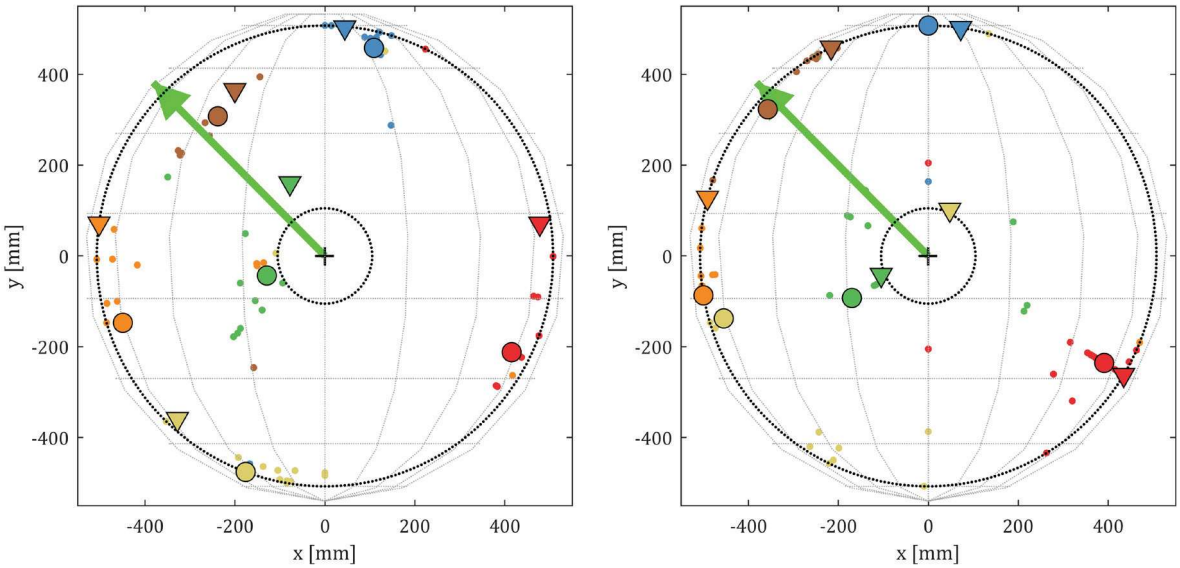

Figure 7 Visualisation of the optimised camera views projected on the x-y-plane at excitation wavenumbers 18787.802 cm^{-1} (left), 18788.456 cm^{-1} (Right). Dotted markers represent all camera positions of the Pareto-optimal set of solutions. Positions highlighted by circle and triangle symbols correspond to the solutions determined according to the velocity and temperature criteria. The black dotted lines mark constraints imposed by the test rig geometry.

on the achievable flow parameter sensitivities as well as to compare the two detection system variants of Figure 1, optimisation results are analysed for configurations with one acquisition channel and six camera views (Cam. 1) and two acquisition channels and four camera views (Cam. 2) with linear (a, c) and circular (b, d) polarised laser radiation. Details on the configurations are summarised in Figure 5.

A comparison of the resulting flow parameter sensitivities is provided in Figure 8. Overall, configurations a) and b) with six camera views show superior results to both configurations with four camera views. Although the number of eight compared to six detected intensity values per resolution element for configurations c) and d) using two acquisition channels is higher, the two additional camera views in configurations a) and b) allow for a stronger variation of the observation directions. This leads to the conclusion that the additional diversity in scattering geometry is preferable to splitting the same collected Rayleigh intensity between two separate iodine filter/camera combinations. Regarding the state of polarisation of the incident laser, no benefit in terms of flow parameter sensitivities can be observed. While results of configurations c) and d) are of similar quality, configuration a) is superior to configuration b) for all flow quantities. The dipole nature of the Rayleigh scattering from linearly polarised laser light and the associated angular signal dependence leads to a stronger variation between the detected signal intensities

compared to the circularly polarised case. This additional signal dynamics achieved for linear polarisation is apparently more beneficial for flow parameter sensitivities than the evenly distributed SNR expected from circular polarisation.

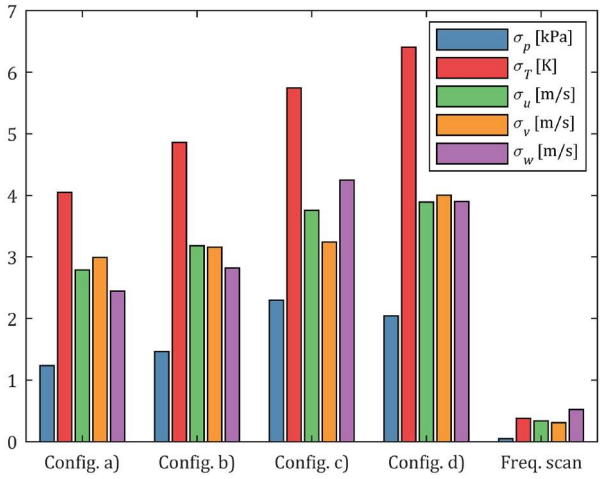

Figure 8 Resulting flow parameter sensitivities for configurations a)-d) at 18788.456 cm^{-1} when applying the velocity criterion. Sensitivities for a typical frequency scan at L2/L3 using are shown right.

To finally compare the single frequency setup for instantaneous and the frequency scanning technique for time-averaged measurements, the scattering geometry obtained at an excitation wavenumber of 18788.456 cm^{-1} for configuration a) with velocity criterion is used to determine the flow parameter sensitivities for a typical wavenumber range and resolution (see e.g. (Doll, Stockhausen, & Willert, 2017)) at absorption lines L2/L3. The corresponding results are depicted in the last column of Figure 8. As stated in the introduction, frequency scanning leads to a considerable improvement of flow parameter sensitivities; by factor of 20 for pressure, a factor of 9 for temperature for temperature and u and v velocities and a factor of 5 for the w component compared to the best single frequency results of configuration a).

6. Conclusion

Combining the FRS technique with multi-view detection provides a possible pathway for the simultaneous measurement of time-resolved 3C velocity, pressure and temperature fields. In this context, the appropriate placement of the different camera views is imperative. This paper presents a general approach to determine the best set of camera views to achieve the highest flow parameter sensitivities using multi-objective optimisation. A multitude of influencing variables from the areas of equipment, test rig and flow properties are identified, which result in a complex system of interdependencies in relation to the measured FRS signal. To keep the problem manageable, equipment specific parameters such as wavenumber and polarisation state of the laser excitation, iodine filter properties as well as the variant of the detection system with one or two acquisition channels using six or four camera views are predefined and combined into different configurations. For each of these configurations, the optimisation routine is then used to determine the optimal combination of camera views within the limits imposed by the geometrical constraints.

When processing the optimisation results, a velocity and a temperature criterion are applied to the Pareto-optimal solution sets to determine the best experimental configuration for the designated flow case. It is revealed that the use of linearly polarised laser light leads to higher flow parameter sensitivities due to the stronger dynamics of the FRS signal compared to circular polarisation. In addition, the use of a single camera/iodine filter combination proves superior to the detection system variant with two acquisition channels, even though the number of detected intensity values is lower. This is possibly related to the larger signal variation that can be achieved by a larger number of perspective views rather than by observing the same scene through different iodine filter cells. It is concluded that linearly polarised laser light combined with an excitation wavenumber of 18788.456 cm^{-1} leads to the highest flow parameter sensitivities for all configurations investigated. As expected, frequency scanning considerably increases the achievable sensitivities.

Future work will focus on the realisation of the presented detection concept. First tests will involve the use of continuous wave laser light, which will allow for a thorough experimental characterisation of the optimised multiple-view setup. Eventually, this will form the basis for the combined measurement of planar 3C velocity, pressure and temperature fields by FRS for the first time.

Acknowledgements

The SINATRA project leading to this publication has received funding from the Clean Sky 2 Joint Undertaking (JU) under grant agreement No 886521. The JU receives support from the European Union's Horizon 2020 research and innovation programme and the Clean Sky 2 JU members other than the Union.

References

Boguszko, M. G. (2003). *Measurement of fluid flows using filtered Rayleigh scattering* [Ph.D thesis]. Rutgers State University.

Charrett, T. O. H., Nobes, D. S., & Tatam, R. P. (2007). Investigation into the selection of viewing configurations for three-component planar Doppler velocimetry measurements. *Applied Optics*, *46*(19), 4102–4116. https://doi.org/10.1364/AO.46.004102

Collette, Y., & Siarry, P. (2004). *Multiobjective Optimization*. Springer Berlin Heidelberg. https://doi.org/10.1007/978-3-662-08883-8

Doll, U., Burow, E., Beversdorff, M., Stockhausen, G., Willert, C., Morsbach, C., Schlüß, D., & Franke, M. (2015). The flow field inside a Ranque-Hilsch vortex tube part I: Experimental analysis

using planar filtered Rayleigh scattering. *9th International Symposium on Turbulence and Shear Flow Phenomena*, *2*.

Doll, U., Burow, E., Stockhausen, G., & Willert, C. (2016). Methods to improve pressure, temperature and velocity accuracies of filtered Rayleigh scattering measurements in gaseous flows. *Measurement Science and Technology*, *27*(12), 125204. Scopus. https://doi.org/10.1088/0957-0233/27/12/125204

Doll, U., Dues, M., Bacci, T., Picchi, A., Stockhausen, G., & Willert, C. (2018). Aero-thermal flow characterization downstream of an NGV cascade by five-hole probe and filtered Rayleigh scattering measurements. *Experiments in Fluids*, *59*(10), 150. https://doi.org/10.1007/s00348-018-2607-z

Doll, U., Fischer, M., Stockhausen, G., & Willert, C. (2012). Frequency scanning filtered Rayleigh scattering in combustion experiments. *16th Int Symp on Applications of Laser Techniques to Fluid Mechanics*. 16th Int Symp on Applications of Laser Techniques to Fluid Mechanics, Lisbon, Portugal.

Doll, U., Stockhausen, G., Heinze, J., Meier, U., Hassa, C., & Bagchi, I. (2017). Temperature measurements at the outlet of a lean burn single-sector combustor by laser optical methods. *Journal of Engineering for Gas Turbines and Power*, *139*(2). Scopus. https://doi.org/10.1115/1.4034355

Doll, U., Stockhausen, G., & Willert, C. (2014a). Endoscopic filtered Rayleigh scattering for the analysis of ducted gas flows. *Experiments in Fluids*, *55*(3), 1690. Scopus. https://doi.org/10.1007/s00348-014-1690-z

Doll, U., Stockhausen, G., & Willert, C. (2014b). Endoscopic filtered Rayleigh scattering for the analysis of ducted gas flows. *Experiments in Fluids*, *55*(3). Scopus. https://doi.org/10.1007/s00348-014-1690-z

Doll, U., Stockhausen, G., & Willert, C. (2017). Pressure, temperature, and three-component velocity fields by filtered Rayleigh scattering velocimetry. *Optics Letters*, *42*(19), 3773–3776. Scopus. https://doi.org/10.1364/OL.42.003773

Forkey, J. N. (1996). *Development and demonstration of filtered Rayleigh scattering: A laser based flow diagnostic for planar measurement of velocity, temperature, and pressure* [Ph.D thesis]. Princeton University.

Forkey, J. N., Finkelstein, N. D., Lempert, W. R., & Miles, R. B. (1996). Demonstration and characterization of filtered Rayleigh scattering for planar velocity measurements. *AIAA Journal*, *34*(3), 442–448. https://doi.org/10.2514/3.13087

Forkey, J. N., Lempert, W. R., & Miles, R. B. (1997). Corrected and calibrated I2 absorption model at frequency-doubled Nd:YAG laser wavelengths. *Applied Optics*, *36*(27), 6729. https://doi.org/10.1364/AO.36.006729

Jainski, C., Lu, L., Sick, V., & Dreizler, A. (2014). Laser imaging investigation of transient heat transfer processes in turbulent nitrogen jets impinging on a heated wall. *International Journal of Heat and Mass Transfer*, *74*, 101–112. https://doi.org/10.1016/j.ijheatmasstransfer.2014.02.072

Klinner, J., & Willert, C. E. (2017). Measurements of Turbulent Jet Mixing in a Turbulent Co-Flow Including the Influence of Periodic Forcing and Heating. *Flow, Turbulence and Combustion*, *98*(3), 751–779. https://doi.org/10.1007/s10494-016-9789-3

Lee, H., Böhm, B., Sadiki, A., & Dreizler, A. (2016). Turbulent heat flux measurement in a non-reacting round jet, using BAM:Eu2+ phosphor thermography and particle image velocimetry. *Applied Physics B*, *122*(7), 209. https://doi.org/10.1007/s00340-016-6484-y

McManus, T. A., & Sutton, J. A. (2020). Simultaneous 2D filtered Rayleigh scattering thermometry and stereoscopic particle image velocimetry measurements in turbulent non-premixed flames. *Experiments in Fluids*, *61*(6), 134. https://doi.org/10.1007/s00348-020-02973-z

Miles, R. B., Lempert, W. R., & Forkey, J. N. (2001). Laser Rayleigh scattering. *Measurement Science and Technology*, *12*(5), R33–R51. https://doi.org/10.1088/0957-0233/12/5/201

Miles, R., & Lempert, W. (1990). Two-dimensional measurement of density, velocity, and temperature in turbulent high-speed air flows by UV rayleigh scattering. *Applied Physics B Photophysics and Laser Chemistry*, *51*(1), 1–7. https://doi.org/10.1007/BF00332317

Most, D., Dinkelacker, F., & Leipertz, A. (2002). Direct determination of the turbulent flux by simultaneous application of filtered rayleigh scattering thermometry and particle image velocimetry. *Proceedings of the Combustion Institute*, *29*(2), 2669–2677. https://doi.org/10.1016/S1540-7489(02)80325-X

Nobes, D. S., Ford, H. D., & Tatam, R. P. (2003). Planar Doppler velocimetry measurements of flows using imaging fiber bundles. *Optical Diagnostics for Fluids, Solids, and Combustion II*, *5191*, 122–133. https://doi.org/10.1117/12.505842

Nobes, D. S., Ford, H. D., & Tatam, R. P. (2004). Instantaneous, three-component planar Doppler velocimetry using imaging fibre bundles. *Experiments in Fluids*, *36*(1), 3–10. https://doi.org/10.1007/s00348-003-0586-0

Schreivogel, P., Abram, C., Fond, B., Straußwald, M., Beyrau, F., & Pfitzner, M. (2016). Simultaneous kHz-rate temperature and velocity field measurements in the flow emanating from angled and trenched film cooling holes. *International Journal of Heat and Mass Transfer*, *103*, 390–400. https://doi.org/10.1016/j.ijheatmasstransfer.2016.06.092

Schroll, M., Doll, U., Stockhausen, G., Meier, U., Willert, C., Hassa, C., & Bagchi, I. (2017). Flow field characterization at the outlet of a lean burn single-sector combustor by laser-optical methods. *Journal of Engineering for Gas Turbines and Power*, *139*(1). Scopus. https://doi.org/10.1115/1.4034040

Straußwald, M., Abram, C., Sander, T., Beyrau, F., & Pfitzner, M. (2020). Time-resolved temperature and velocity field measurements in gas turbine film cooling flows with mainstream turbulence. *Experiments in Fluids*, *62*(1), 3. https://doi.org/10.1007/s00348-020-03087-2

Su, L. K., & Mungal, M. G. (2004). Simultaneous measurements of scalar and velocity field evolution in turbulent crossflowing jets. *Journal of Fluid Mechanics*, *513*, 1–45. https://doi.org/10.1017/S0022112004009401

Willert, C., Stockhausen, G., Beversdorff, M., Klinner, J., Lempereur, C., Barricau, P., Quest, J., & Jansen, U. (2005). Application of Doppler global velocimetry in cryogenic wind tunnels. *Experiments in Fluids*, *39*(2), 420–430. https://doi.org/10.1007/s00348-004-0914-z